Cell dynamics simulations of shear-induced alignment and defect annihilation in stripe patterns formed by block copolymers

S. R. Ren and I. W. Hamley*
School of Chemistry, University of Leeds, Leeds LS2 9JT, United Kingdom

P. I. C. Teixeira† and P. D. Olmsted
Department of Physics and Astronomy, University of Leeds, Leeds LS2 9JT, United Kingdom

(Received 27 June 2000; revised manuscript received 5 December 2000; published 26 March 2001)

The effect of large amplitude oscillatory shear on two-dimensional stripe patterns formed by block copolymers was investigated using cell dynamics simulations. A global orientational order parameter S and a correlation function for stripe normals $G(\mathbf{r}-\mathbf{r}')$ were used to characterize the degree of stripe orientation under shear. The kinetics of stripe alignment, quantified by S, at various shear and quench conditions were studied as a function of strain amplitude, shear frequency, and temperature. The mechanisms of shear alignment and defect annihilation were investigated. A critical shear condition for complete alignment of stripes along the shear direction was also identified.

DOI: 10.1103/PhysRevE.63.041503 PACS number(s): 83.50.−v, 47.20.Hw, 81.05.Lg, 66.30.Lw

I. INTRODUCTION

Block copolymers have found wide application because their morphology can be systematically modified not only by controlling the composition and segment length of the polymer blocks but also by changing the processing method. In particular, the global orientation and topological defects in a microphase-separated morphology are important factors affecting the optical, permeability, electrical, and mechanical properties of block copolymers. The use of block copolymers in electronic and photonic applications requires the production of highly ordered and defect-free materials [1]. Flow-induced alignment of block copolymer microstructures has been demonstrated for materials subjected to oscillatory or steady shear [2–5], extrusion [6], extensional flow [7,8], and roll casting [8,9]. Alignment and defect removal mechanisms in a lamellar phase induced by an electric field have also been studied in the bulk [10,11]. All of the preceding studies have focused on bulk samples. Alignment in block copolymer films has been achieved using electric fields [12,13], by tuning substrate surface energy [14], and by patterning using self-assembled monolayers [15,16]. Shearing of block copolymers in films between parallel plates is often used to align samples; however, these are usually closer to the bulk three-dimensional limit than the two-dimensional limit.

The structure of defects in block copolymers has been the subject of experimental [17,18] and theoretical [19,20] investigation. The effect of shear on defects has also been studied; in particular, Winey and co-workers have undertaken a comprehensive examination of the effects of steady or large amplitude oscillatory shear on kink bands and tilt grain boundaries [21–23]. The kink bands themselves are generated in a controlled manner through variation of the rate and amplitude of steady shear. The kinetics of alignment (defect elimination) in block copolymers under shear flow have also been probed via rheology and birefringence [24–26] and small-angle scattering experiments [1,4,27,28].

Computer simulation is playing an increasingly important role in understanding the mechanisms of morphology changes in block copolymers. The cell dynamics simulation (CDS) method is a very promising approach to modeling the mesoscopic structure of block copolymers [29–35] and the influence of external fields on morphology. The effect of shear on two-dimensional hexagonal [36] and stripe [37] patterns has previously been investigated by cell dynamics simulations. The effects of both oscillatory and step strain on the hexagonal phase have also been simulated using the cell dynamics method [36]. The relaxation of the shear stress following step strain was analyzed as a function of strain amplitude, and a two-step relaxation process was observed for large strains. After the rapid initial decrease of stress due to relaxation of distorted domains, a plateau was observed followed by another decrease in stress that was ascribed to the slippage of lattice planes. Under oscillatory shear, linear viscoelastic behavior was observed at low strain amplitudes. However, when large amplitude oscillatory shear was applied, a nonsinusoidal stress was found to be out of phase with the applied sinusoidal strain and slip of lattice planes was again inferred [38]. Kodama and Doi [37] performed cell dynamics simulations of stripe patterns under steady shear flow and observed two types of lamellar instability: breakup-recombination and undulation. A stability diagram for these structures was also obtained in terms of a temperaturelike parameter and wave number corresponding to the lamellar period. Drolet, Chen, and Viñals [39] analyzed the stability boundaries of deformed lamellar morphologies under shear via numerical analysis of a linearized version of a Cahn-Hilliard-Cook equation with added convective term. They found that the boundaries are affected by shear amplitude and frequency.

*Author to whom correspondence should be addressed.
†Present address: Departamento de Engenharia de Materiais, Instituto Superior Tecnico, Avenida Rovisco Pais, P-1049-001 Lisbon, Portugal.

We present simulation results for a two-dimensional stripe phase as formed, for example, by symmetric block copolymers (which in bulk would form a lamellar phase). Although our results are presented in terms of the effect of shear on a block copolymer stripe phase, the conclusions should apply for any stripe pattern that can be oriented by shear because the cell dynamics equations are not specific to block copolymers. However, stripe phases in other systems such as type I superconductor films [40], ferromagnetic garnet films [41,42], or Langmuir monolayers of lipid molecules [42] cannot be oriented by shear.

The stripe orientation is characterized using an interface orientational order parameter and an interface normal correlation function. We have investigated the dynamics of stripe alignment under large amplitude oscillatory shear at various shear and quench conditions. A critical condition (shear frequency and amplitude) for complete alignment of the copolymer stripes under oscillatory shear is given. Finally, the process of defect annihilation under shear is investigated.

The paper is organized as follows. In Sec. II, details of the CDS model are provided, followed in Sec. III by a discussion of the results, first introducing measures of the orientational order of stripes and a correlation function for stripe orientation. Then the dynamics of shear-induced alignment as a function of temperature and the frequency and amplitude of oscillatory shear are investigated. We then identify a critical condition for shear-induced parallel alignment of stripes. The nature of the defect structures in the stripe pattern and the effects of thermal annealing and shearing on defect annihilation are then considered, as are the effect of system size and simulation time step. Finally, conclusions are summarized.

II. THE CDS MODEL

In the cell dynamics method, an appropriate order parameter takes values $\psi(t,i)$ in cell i of a discrete lattice at time t. For an AB diblock copolymer a suitable choice is the compositional order parameter

$$\psi(\mathbf{r}) = \phi_A(\mathbf{r}) - \phi_B(\mathbf{r}) + (1-2f), \tag{1}$$

where $\phi_A(\mathbf{r})$ and $\phi_B(\mathbf{r})$ are the local volume fractions of blocks A and B, and f is the block length ratio.

We consider first dynamical equations in the absence of shear. The cell dynamics equations for a conserved order parameter, appropriate for a block copolymer, can be shown to correspond to a coarse-grained discretization of the Cahn-Hilliard-Cook equation [43],

$$\frac{\partial \psi}{\partial t} = M\nabla^2\left(\frac{\delta F(\psi)}{\delta \psi}\right) + \eta\xi(\mathbf{r},t), \tag{2}$$

where M is a phenomenological mobility constant and η is the amplitude of thermal noise. Here we set $M=1$ which correspondingly sets the time scale for diffusive processes. Also in Eq. (2) $\xi(\mathbf{r},t)$ is a Gaussian random noise term, satisfying the fluctuation-dissipation theorem, in this case

$$\langle \xi(\mathbf{r},t)\rangle = 0,$$

$$\langle \xi(\mathbf{r},t)\xi(\mathbf{r},t)\rangle = -2k_BTM\nabla^2\delta(\mathbf{r}-\mathbf{r}')\delta(t-t'). \tag{3}$$

Here k_B is Boltzmann's constant and T denotes the temperature. The fluctuation-dissipation theorem is satisfied for $\eta=1$, but for other values the noise has arbitrary strength. In Eq. (2), $F(\psi)$ is the free energy functional, consisting of short range and long range interaction terms:

$$F(\psi) = F_S(\psi) + F_L(\psi). \tag{4}$$

The short range interaction term is written as [30]

$$F_S(\psi) = \int d\mathbf{r}\left(H(\psi) + \frac{D}{2}[\nabla\psi(\mathbf{r})]^2\right), \tag{5}$$

where D is a phenomenological constant that controls the free energy penalty for spatial composition heterogeneity, and $H(\psi)$ is a free energy functional that has two minima in an ordered phase which can be written as [33]

$$H(\psi) = \left(-\frac{\tau}{2} + \frac{A}{2}(1-2f)^2\right)\psi + \frac{v}{3}(1-2f)\psi^3 + \frac{u}{4}\psi^4. \tag{6}$$

Here τ is a temperaturelike parameter and A, v, and u are phenomenological constants. The long range interaction term in Eq. (4) is given by [44]

$$F_L(\psi) = \frac{B}{2}\int d\mathbf{r}_1 \int d\mathbf{r}_2 G(\mathbf{r}_1-\mathbf{r}_2)[\psi(\mathbf{r}_1)-\overline{\psi}][\psi(\mathbf{r}_2)-\overline{\psi}], \tag{7}$$

where $G(\mathbf{r}_1-\mathbf{r}_2)$ is the Green's function for the Laplace equation $\nabla^2 G(\mathbf{r}_1-\mathbf{r}_2) = -\delta(\mathbf{r}_1-\mathbf{r}_2)$. The parameters D, B, and τ may be related to polymer characteristics, such as the degree of polymerization N, the segment length b, and the Flory-Huggins interaction parameter [36,37].

We now turn to a description of the dynamics of a block copolymer in the presence of a flow field, neglecting hydrodynamics. The time evolution of the order parameter under a macroscopic shear flow is given by a CHC equation modified by addition of a convective term [36,37],

$$\frac{\partial \psi}{\partial t} + \nabla\cdot(\mathbf{v}\psi) = M\nabla^2\left(\frac{\delta F(\psi)}{\delta\psi}\right) + \eta\xi(\mathbf{r},t), \tag{8}$$

where $\mathbf{v}=(v_x,v_y,v_z)$ is the flow field. We consider oscillatory shear flows defined by

$$v_x = \dot{\gamma}(t)y, \quad v_y = v_z = 0, \tag{9}$$

where $\gamma(t)=\gamma_a\sin(\omega t)$. Writing $g(\psi)=dH(\psi)/d\psi$, Eq. (8) thus becomes

$$\frac{\partial\psi}{\partial t} = -\dot{\gamma}y\frac{\partial\psi}{\partial x} + \nabla^2\psi - \nabla^2[g(\psi) + D\nabla^2\psi] - B\psi + \eta\xi. \tag{10}$$

Cell dynamics simulations correspond to coarse-grained discretizations of the Cahn-Hilliard-Cook (or time-dependent Ginzburg-Landau) equation. The method is no less realistic

than direct numerical integration of the partial differential equations, and provides significant computational advantages [43]. This allows easier exploration of the late-time regime of phase ordering. Furthermore, it has been shown that the CDS method has essentially the same dynamical scaling properties as the CHC equation, and is therefore a reliable tool for its elucidation [43].

The discrete cell dynamics equation corresponding to this expression used in the simulations is [30,36],

$$\psi(n,t+\Delta t)=\psi(n,t)-\Delta t\{\langle\langle\Gamma(n,t)\rangle\rangle-\Gamma(n,t)+B\psi(n,t) - \eta\xi(n,t)+\tfrac{1}{2}\dot{\gamma}y[\psi(n_x+1,ny,t) - \psi(n_x-1,n_y,t)]\}. \tag{11}$$

Here Δt is the time step

$$\Gamma(n,t)=g(\psi(n,t))-\psi(n,t)+D[\langle\langle\psi(n,t)\rangle\rangle-\psi(n,t)], \tag{12}$$

where the map function used was [35]

$$g(\psi)=[1+\tau-A(1-2f)^2]\psi-v(1-2f)\psi^2-u\psi^3. \tag{13}$$

This polynomial form differs from the usual symmetric function $g(\psi)=A\tanh(\psi)$ used in cell dynamics simulations [43,45], because it is necessary to include a cubic term in Eq. (6) to account for the formation of hexagonal and cubic phases when using a Landau free energy.

In the present study, the stripe phase was simulated for a diblock copolymer with $f=0.5$. Sheared periodic boundary conditions were used [36]. The simulations were performed with the following parameters: $D=0.5$, $B=0.02$, $u=0.5$, and $v=1.5$. The results presented herein were obtained for a 128×128 lattice. However, we have also performed simulations on a 256×256 lattice. The ordering kinetics are found to be the same, provided that the time step is rescaled, as discussed in Sec. III G below. The noise amplitude was zero except where stated.

III. RESULTS AND DISCUSSION

A. Characterization of copolymer stripes

The degree of alignment of the stripes is quantified using the two-dimensional nematic orientational order parameter,

$$S=\langle 2\cos^2\theta-1\rangle, \tag{14}$$

where θ is the angle between the unit normal vector of the stripes and the unit normal vector in the direction of the applied shear field. The spatial average takes the value $S=0$ for an isotropic phase, and $S=1$ for a completely oriented phase.

To quantify the correlation of stripe orientation over different length scales, and therefore characterize the effect of defects on the morphology, a correlation function for the stripe normal $\mathbf{n}(\mathbf{r})$ at the interface between A and B stripes was introduced:

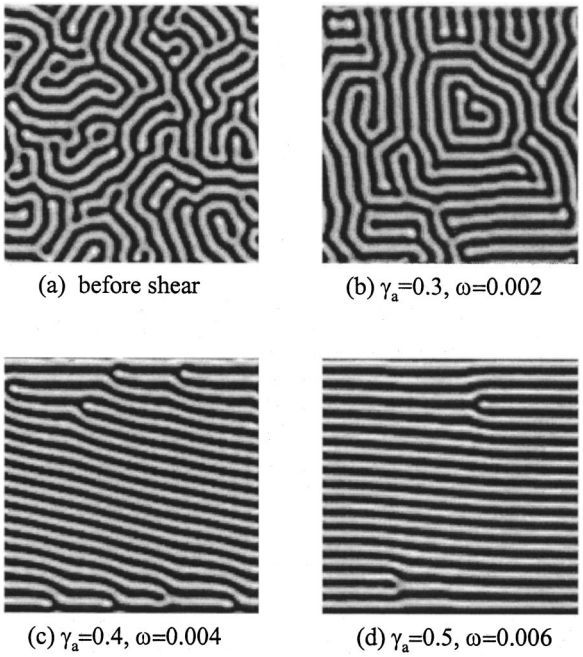

FIG. 1. Stripe morphology achieved after prolonged oscillatory shear under various shear conditions, as indicated ($\tau=0.35$).

$$G(\mathbf{r}-\mathbf{r}')=\langle|\mathbf{n}(\mathbf{r})\cdot\mathbf{n}(\mathbf{r}')|\rangle=\langle e^{i2\theta(\mathbf{r})}e^{-i2\theta(\mathbf{r}')}\rangle =\langle 2\cos^2\beta-1\rangle, \tag{15}$$

where β is the angle between the unit normal vectors and $\langle\,\rangle$ denotes a spatial average. For the discrete stripes in the simulation, β (equal to $n\pi/4$, $n=0,1,2,...,7$) was computed with respect to the vector between adjacent cells at the stripe boundary. For small $r=\mathbf{r}-\mathbf{r}'$, $G(\mathbf{r}-\mathbf{r}')$ is strongly dependent on local stripe shape and orientation. For larger $\mathbf{r}-\mathbf{r}'$, $G(\mathbf{r}-\mathbf{r}')$ approaches its value for random stripe orientation (equal to zero). For complete alignment along the shear direction, $G(\mathbf{r}-\mathbf{r}')$ approaches 1. Therefore, the interface normal correlation function depends on the spatial extent and density of defects.

B. Dynamics of stripe alignment

Results from a simulation where large amplitude oscillatory shear was applied to a macroscopically disordered stripe pattern (generated from an initially random disordered state) are shown in Fig. 1. Figure 1(a) is an unsheared stripe pattern. Figures 1(b)–1(d) contain stripe patterns generated after 5×10^5 time steps under oscillatory shear for different combinations of amplitude and frequency. Figure 2 shows the time development of the orientational order parameter S for the same conditions as in Fig. 1; however, the mean order parameter was computed from seven independent runs. As seen in Fig. 2, S reaches a constant value for all cases studied, confirming that a steady state has been reached. It was noted that the pattern was not static, even though S remained at its plateau value. Instead, the defect pattern moved around, but could not be annihilated under the strength of the shear field applied even after 7×10^5 time steps. In the cases

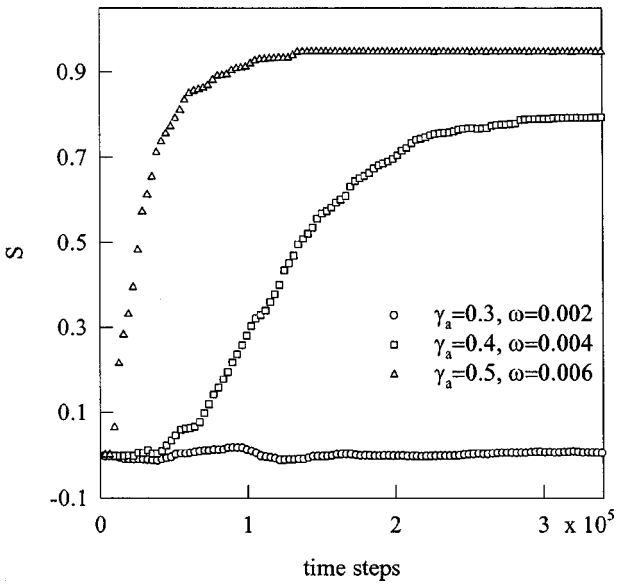

FIG. 2. Alignment kinetics under the shear conditions shown in Fig. 1. The curves correspond to parts (b)–(d) in Fig. 1.

shown in Figs. 1(b), 1(c), and 1(d) only partial alignment of the stripes is attained, in which many defects, such as dislocations, disclinations, and sharp bends, are retained. The defect density varies with the shear amplitude and frequency applied. Saturation of alignment is achieved only above a threshold shear condition [such as shear amplitude $\gamma_a = 0.5$, frequency $\omega = 0.006$, as shown in Fig. 1(d)]. The time to reach saturated alignment depends on shear conditions. In general, a stronger shear field (larger amplitude and higher frequency) causes the plateau to be reached sooner.

The effect of the coupling between shear and temperature was also explored. Figure 3 shows the effect of the temperaturelike parameter τ (related to quench depth) on the alignment dynamics of the stripe system under fixed conditions of

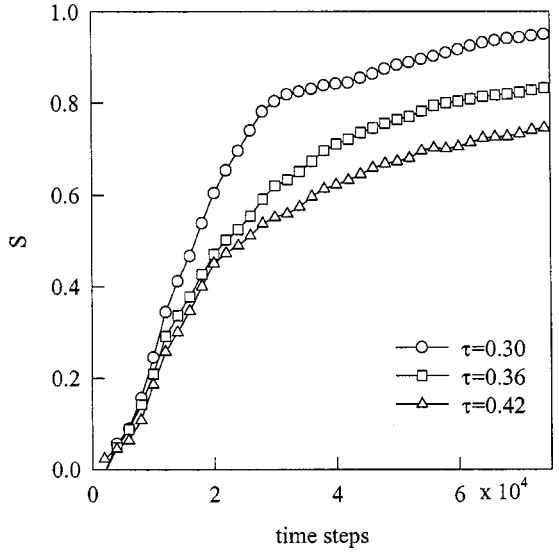

FIG. 3. Alignment kinetics for different quench temperatures τ. Oscillatory shear ($\gamma_a = 0.5$, $\omega = 0.007$) was applied *after* the evolution of an unaligned structure.

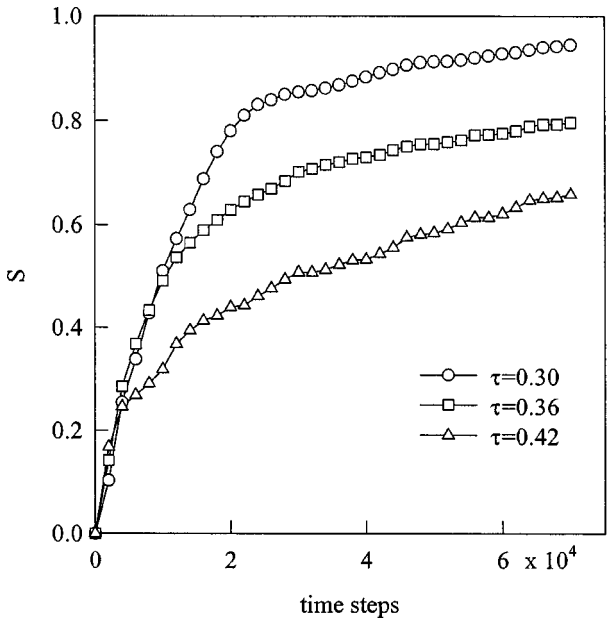

FIG. 4. Alignment kinetics for different quench temperatures τ. Oscillatory shear ($\gamma_a = 0.5$, $\omega = 0.007$) was applied *during* the evolution of the structure.

oscillatory shear ($\gamma_a = 0.5$, $\omega = 0.007$). Three cases with different τ values ($\tau = 0.30$, 0.36, and 0.42) were simulated with the thermal noise amplitude $\eta = 0$. In the simulation, a steady state unaligned stripe pattern was first generated from an initially random disordered state. Oscillatory shear was then applied to the system at constant τ during the pattern evolution. The data (obtained from at least five independent runs) reveal that, as the quench deepens (larger τ values), the system becomes less susceptible to shear orientation, and a lower degree of alignment and more defects were found following shear. Alignment is also slower for a deeper quench. The development of the order parameter when shear was applied from the start of the quench (i.e., at $t = 0$ the system was in the isotropic state) is shown in Fig. 4 for the same quench depths as Fig. 3, and again using an average over at least five independent runs. In general, the order parameter kinetics (and saturation value of S) are not strongly dependent on the path, i.e., the time at which shear is applied.

C. Critical shear conditions for parallel alignment

Figure 5 shows the steady state value of S as a function of shear amplitude at two different frequencies ($\omega = 0.0015$ and 0.0035 for $\tau = 0.35$). The oscillatory shear was applied after the steady state structure was formed (about 3×10^4 time steps). The runs were continued until the alignment saturated (between 10^5 and 10^6 time steps) and the data points shown in the figure are averages from at least three independent runs. The data reveal that at a fixed frequency the orientational order parameter S gradually increases with increasing shear amplitude until complete alignment is achieved at a critical value of the shear amplitude. This critical value is dependent on shear frequency: at a higher frequency, a lower shear amplitude was needed to align the stripes completely.

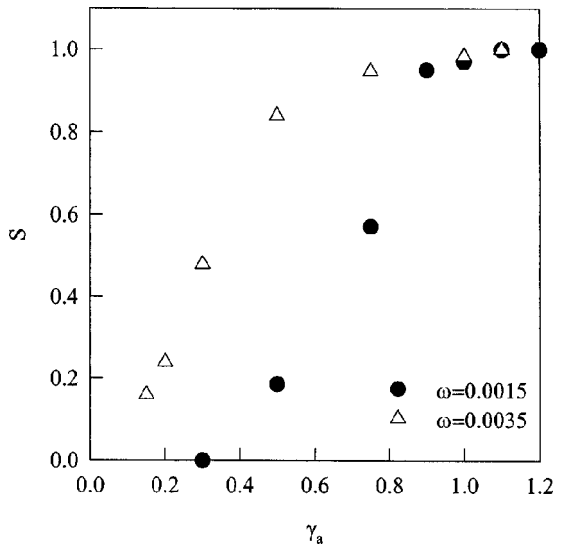

FIG. 5. The steady state orientational order parameter plotted against shear amplitude for shear frequencies $\omega=0.0015$ and 0.0035 ($\tau=0.35$).

Representative results showing the dependence of S on frequency for different shear amplitudes are shown in Fig. 6. In contrast to the smooth dependence of S on strain amplitude, the orientational order parameter increases sharply at a critical frequency above which complete alignment is achieved for sufficiently large strains, the magnitude of the critical frequency depending on strain.

The critical shear amplitude versus critical oscillatory frequency for achieving essentially complete stripe alignment is shown in Fig. 7. The data were obtained from a series of simulations for different shear amplitude and frequency combinations. Complete alignment was defined for S greater than 0.97, where all the stripes in the system were aligned in the shear direction, and the number of defects (such as a dislocation or a disclination) left was less than 2. The data were

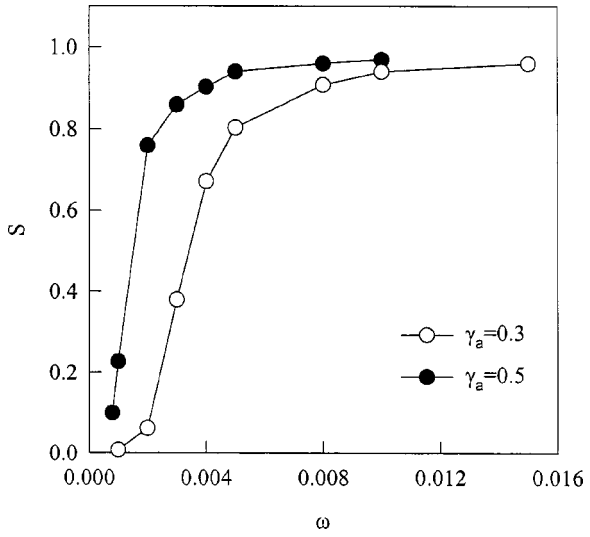

FIG. 6. The steady state orientational order parameter plotted against shear frequency for shear amplitudes $\gamma_a=0.3$ and 0.5 ($\tau=0.35$).

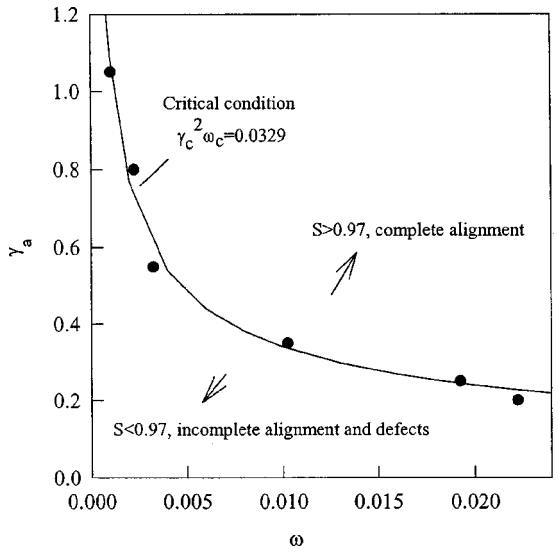

FIG. 7. Shear amplitude versus frequency, showing the critical shear condition to achieve complete stripe alignment. The points shown are from the simulations, and the solid line is a fitted function.

fitted with a power-law equation, leading to a critical condition for alignment,

$$\gamma_c^2\omega_c=\text{const}, \tag{16}$$

where γ_c and ω_c are the critical shear amplitude and frequency, respectively.

To understand the critical alignment condition, consider the balance of convective and diffusive effects for a grain of lamellae. The balance of these two effects leads to

$$\gamma_a\omega\frac{d\psi}{dx}\sim\frac{d^2\psi}{dx^2}, \tag{17}$$

where $\gamma_a=dv_x/dy$ is the magnitude of the imposed strain. This leads to the condition

$$\gamma_a\omega l_x\sim 1, \tag{18}$$

where l_x is a characteristic distance along the flow direction. If we consider the motion of successive layers along the y direction, so that $dy\sim d$ ($d=$layer spacing), the characteristic distance is obtained from $\gamma_a\sim l_x/d$, leading to

$$\gamma_a^2\omega\sim 1/d^2. \tag{19}$$

The quantity on the right-hand side is a constant for a particular system size, so that Eq. (19) is equivalent to Eq. (16) at the critical strain and frequency. This argument suggests that shear alignment results predominantly from the balance of convection and diffusion.

The shape of the critical strain-frequency curve obtained from the CDS simulation for complete stripe alignment (Fig. 7) is remarkably similar to that observed in large amplitude oscillatory shear experiments on (three-dimensional) lamellar block copolymers [46]. There, the transition is from a parallel orientation (with respect to the shear plane) to a per-

pendicular orientation upon either increasing strain amplitude at a fixed frequency or vice versa. Obviously the mechanisms of flow in two and three dimensions are different, especially since layers sliding over one another are not observed in the two-dimensional system. The correspondence between the shape of the critical strain-frequency curve in Fig. 7 and the results of experiments on bulk lamellar samples may therefore be fortuitous. The next important task for modeling is to simulate the effect of shear on three-dimensional lamellar phases, and work on this is in progress. Further work will also examine the influence of hydrodynamics on defect motion, i.e., cell dynamics simulations will be performed corresponding to Model H rather than Model B (Cahn-Hilliard-Cook) in the Hohenberg-Halperin classification [47].

D. Defect structure

The stripe patterns formed for systems below the critical strain/frequency condition contain multiple defects, which are two-dimensional point defects. A discontinuity in the position of a stripe leads to a dislocation. A discontinuity in stripe orientation leads to a disclination, of which both $s=\frac{1}{2}$ and $-\frac{1}{2}$ are observed, where s is the disclination ''strength'' [48,49]. Line defects are also observed (analogous to wall defects in three dimensions). In the shear-aligned stripe pattern shown in Fig. 1(d), two defect structures can be observed by looking at the ''white'' stripes. In the right top corner, a dislocation is evident, and in the bottom left corner an $s=-\frac{1}{2}$ disclination can be seen. These two typical defect structures can be traced back to the original pattern—the macroscopically unaligned structure, as shown in Fig. 1(a). A broken (or isolated ''white'') stripe may form a dislocation under shear, while a branched stripe may be stretched to form a disclination. These two defects can convert into each other as a result of continuous movement of the dislocation or disclination lines under internal (e.g., temperature fluctuation) or external (e.g., shear or electric field) fields. This phenomenon was described as defect line climb or glide by Amundson *et al.* [11]. Figure 1(c) contains good examples of lines of defects. In particular, at the top and bottom lines of dislocations can be identified.

The effect of thermal history on quenched defects was also examined, in the absence of both shear flow and random thermal noise. Figure 8 shows examples of stripe patterns formed along different quench paths. All patterns correspond to steady state structures, i.e., S had saturated at a constant value for at least 3×10^4 time steps. In Figs. 8(a)–8(c), the structures were formed by direct quench to $\tau=0.30$, 0.35, and 0.42, respectively, from an initially unaligned configuration. The pattern shown in Fig. 8(d) was simulated for a different τ path. First, a pattern was generated at $\tau=0.42$. Then a second quench was imposed on the pattern by changing τ to 0.30, until a steady state was reached. As expected, the pattern for the deeper quench, Fig. 8(c), has higher defect density than any other pattern, as quantified by the number of broken, branched, and isolated short stripes. The indirect path, i.e., initial quenching to a lower temperature, then increasing temperature [Fig. 8(d)], leads to a higher defect density than the direct path [Fig. 8(a)], as the trapped defects from the intial quench are not totally annealed out. The orientational order parameter S is unsuitable to quantify the degree of alignment in these patterns because the (nearly circular) symmetry is not broken by application of an external field. Thus instead we exploit the interface normal correlation function $G(\mathbf{r}-\mathbf{r}')$ defined in Sec. III A. Figure 9 shows the computed $G(\mathbf{r}-\mathbf{r}')$ for each pattern and highlights significant differences of $G(\mathbf{r}-\mathbf{r}')$ for the four quench

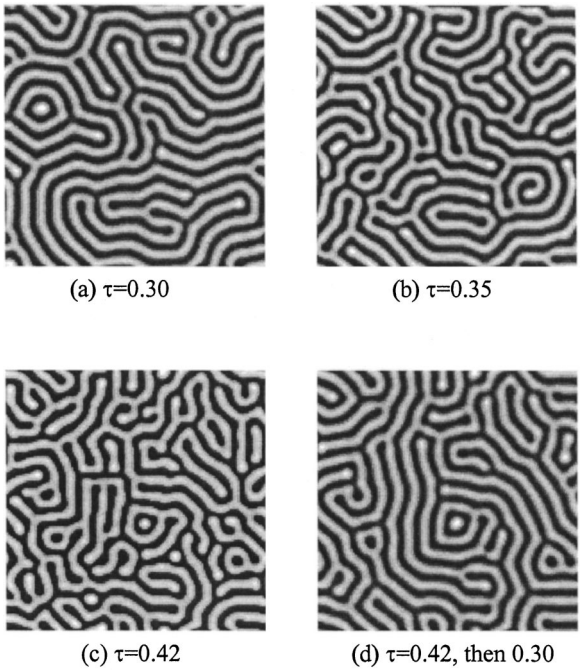

FIG. 8. Stripe structures showing quenched defects developed for different thermal histories, starting from an initial random disordered state. All simulations were performed without shear.

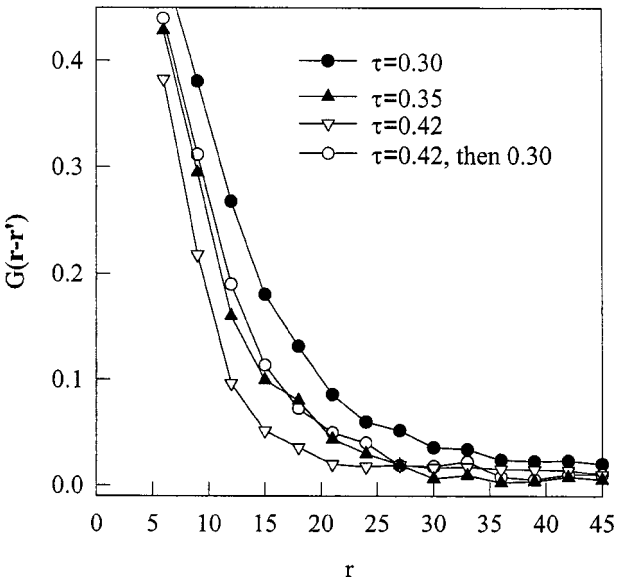

FIG. 9. The correlation function $G(\mathbf{r}-\mathbf{r}')$ of the stripe normals calculated for the four structures shown in Fig. 8.

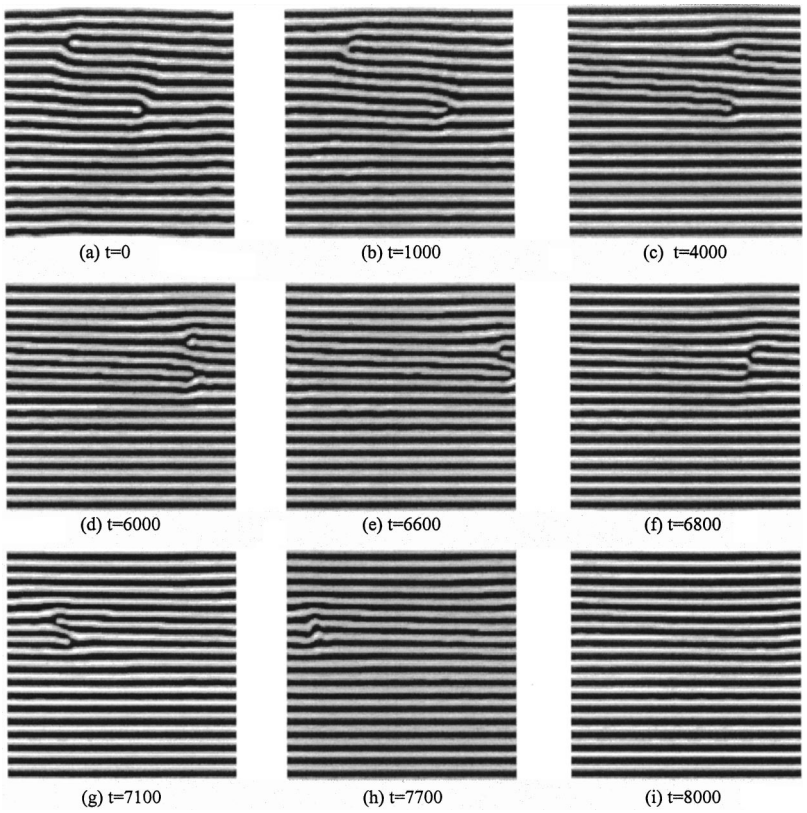

FIG. 10. Defect annihilation process under shear. The images show the intermediate defect structures during shear ($\gamma_a = 0.6$, $\omega = 0.01$) for a series of time steps from a single simulation run. The initial configuration in (a) was achieved following shear at $\gamma_a = 0.5$, $\omega = 0.01$ (for $t = 1.1 \times 10^4$ time steps).

paths, particularly at small r. This is due to the presence of localized defect structures. The correlation function shows quantitatively that a lower defect density is attained via a direct quench to $\tau = 0.30$ than by an indirect thermal path, via an initially deeper quench.

E. Defect annihilation under shear

Stripe alignment under oscillatory shear is achieved through stripe stretching and defect annihilation. Fig. 10 shows a series of frames to demonstrate the process of defect removal. A typical pattern with two dislocations, which was produced following shear at $\gamma_a = 0.5$, and $\omega = 0.01$ for 1.1×10^4 time steps ($\Delta t = 1$), was selected as an initial state of the pattern [Fig. 10(a)]. A stronger shear field ($\gamma_a = 0.6$, $\omega = 0.01$) was then applied. The intermediate structures formed during shear were captured at several time steps. After 1000 time steps of shear, the top dislocation defect was converted into a disclination, apparently due to one end of the dislocated stripe moving down to join with its neighbor. Meanwhile, the bottom defect shifted to the right. After 4000 time steps, a dislocation was formed again at a new position to the right of the disclination that was destroyed. The defect pairs were brought closer and closer through this dislocation-disclination conversion during the shear, as shown in stages 10(d) to 10(f). Eventually, two dislocated stripes were brought together [Fig. 10(g)], connected [Fig. 10(h)], and straightened. Stripe alignment was completed after 8800 time steps [Fig. 10(i)].

Many mechanisms have been proposed for flow-induced alignment and defect annihilation in lamellar phases [25]. These include domain dissolution, grain rotation, selective melting, and defect migration. Supported by small-angle neutron scattering (SANS) and *in situ* rheo-optical measurements, Chen and Kornfield observed that defect migration was responsible for lamellae alignment under oscillatory shear in the low frequency regime [25]. The breaking and reforming of lamellae through the movement of dislocations and disclinations were observed. This is in accord with observations from our simulations. These show that defect annihilation is caused by the movement of defects along the shear direction and migration perpendicular to the shear direction due to microstructure relaxation. These two effects bring the defects closer to each other, before they eventually join and are annihilated.

F. Effect of thermal noise on defects

In the preceding simulations, thermal noise was not included. In separate simulations, the effect of addition of thermal noise to a presheared system was investigated. In Eq. (11), η was fixed at a nonzero value. To ensure approximate conservation of the order parameter when noise is added we have adapted a procedure described elsewhere [50]. Specifically, two independent Gaussian distributed random numbers $\xi_l(i,j)$ and $\xi_m(i,j)$ are generated at each lattice point (i,j), representing fluctuations in different directions. The noise term is then taken as $\eta\xi(r,t) = \eta[\xi_l(i,j) - \xi_l(i \pm 1,j) + \xi_m(i,j) - \xi_m(i,j \pm 1)]$ at each time step. A third set of uniformly distributed random nubmers is used to determine whether $\pm$ is $+$ or $-$ in the calculation. Increasing noise

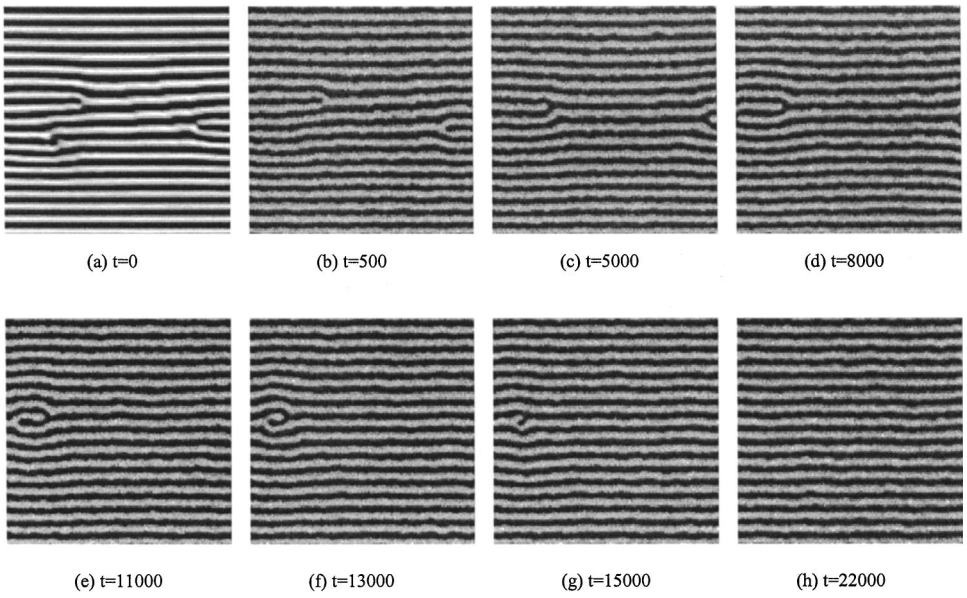

FIG. 11. Defect annihilation during thermal annealing ($\tau = 0.35$, noise added, amplitude $\eta = 0.1$) in the absence of shear. The evolution of defect structures was captured at several time steps during a simulation run.

amplitude leads to a coarsening of the domain structure [51] and enhanced lamellar orientation due to local thermal annealing, up to some critical value of η above which the system becomes disordered.

Patterns that illustrate the effect of noise on the removal of defects are illustrated in Fig. 11. The initial state was selected from a shear-aligned structure, which contains a pair of disclinations and two stripes with a small bend. Noise was then added to the system in the absence of shear. After 500 time steps, the disclinations were converted into dislocations, and the bends in two stripes disappeared [Fig. 11(b)]. The defects then moved closer together [Fig. 11(c)–11(g)] until finally no defects remained after 2.2×10^4 time steps. Thus, thermal noise acted to mobilize the stripes and facilitate the migration of defects toward each other. In other words, it acts to enhance the annealing of defects. In separate runs, it was also observed that there exists a critical noise level, similar to the shear amplitude and frequency, to annihilate the defects.

G. Effect of system size and time step

To check the influence of system size, simulations were run on a 256×256 lattice as well as a 128×128 lattice. The order parameter S increased more rapidly with time for the larger system, although the same steady state value of S was eventually obtained as for the smaller system. The difference in ordering kinetics can be understood to result from the increase in the strain at the moving edge of the simulation box for the larger system compared to the small one [Eq. (19)].

In its original implementation [43], the cell dynamics method was based on a time step $\Delta t = 1$ [see Eq. (11)]. However, we found that results for the kinetics of order parameter development performed for different time steps were superimposable only with $\Delta t < 0.5$. When shear was applied, it was found that the time step had to be reduced further to achieve convergent results. In the case of oscillatory shear, smaller time steps were needed than for steady shear. The time step was found to have a significant effect on the kinetics of alignment, but little effect on the final state of alignment. To achieve a balance between reasonable simulation run times and accuracy of the order parameter kinetic profiles, time steps in the range $\Delta t = 0.1-0.2$ were used for the oscillatory shear simulations in this study.

IV. CONCLUSIONS

The critical shear conditions for achieving complete alignment of morphology are of practical importance in locating processing parameters for a block copolymer. The kinetics of alignment are also important, since they provide the basis for estimating the processing time to reach a well-aligned structure. The degree of orientation and density of defects can strongly affect the performance of well-aligned samples. Cell dynamics simulations can play an important role in elucidating all three of these effects.

Our simulations indicated that large amplitude oscillatory shear can induce alignment of a stripe phase along the shear direction. The degree of the stripe orientation induced by shear depends on the shear conditions. To achieve complete stripe alignment along the shear direction, a critical shear field, in which shear amplitude and frequency follow a power-law coupling, must be applied, otherwise only partial alignment can be obtained. The kinetics of shear alignment also depend on the shear condition and quench temperature. In particular, a steady state is reached more rapidly at higher frequencies and for shallower thermal quenches. Increasing the amplitude of oscillatory shear leads to enhanced orientational order, although the kinetics are not strongly dependent on strain amplitude.

Edge dislocations, $s = \pm\frac{1}{2}$ disclinations, and stripe bend walls were observed as the main types of morphological defect appearing in the simulated block copolymer structures.

Defect annihilation under oscillatory shear is due to stripeorientation in the shear direction and defect mobilization that leads to the approach of defects, eventually reforming the stripes. Finally, increasing thermal fluctuations or temperature significantly reduce the defect density.

ACKNOWLEDGMENT

This work was supported by the Engineering and Physical Sciences Research Council, U.K. (Grant No. GR/M08523 to I.W.H.).

[1] H. Wang, M. C. Newstein, A. Krishnan, N. P. Balsara, B. A. Garetz, B. Hammouda, and R. Krishnamoorti, Macromolecules **32**, 3695 (1999).
[2] G. H. Fredrickson and F. S. Bates, Annu. Rev. Mater. Sci. **26**, 501 (1996).
[3] U. Wiesner, Macromol. Chem. Phys. **198**, 3319 (1997).
[4] Z.-R. Chen, J. A. Kornfield, S. D. Smith, J. T. Grothaus, and M. M. Satkowski, Science **277**, 1248 (1997).
[5] I. W. Hamley, *The Physics of Block Copolymers* (Oxford University Press, Oxford, 1998).
[6] A. Keller, E. Pedemonte, and F. M. Willmouth, Nature (London) **225**, 538 (1970).
[7] H. H. Lee, R. A. Register, D. A. Hajduk, and S. M. Gruner, Polym. Eng. Sci. **36**, 1414 (1996).
[8] C. C. Honeker and E. L. Thomas, Chem. Mater. **8**, 1702 (1996).
[9] R. J. Albalak and E. L. Thomas, J. Polym. Sci., Part B: Polym. Phys. **31**, 37 (1993).
[10] K. Amundson, E. Helfand, X. Quan, and S. D. Smith, Macromolecules **26**, 2968 (1993).
[11] K. Amundson, E. Helfand, X. Quan, S. D. Hudson, and S. D. Smith, Macromolecules **27**, 6559 (1994).
[12] T. L. Morkved, M. Lu, A. M. Urbas, E. E. Ehrichs, H. M. Jaeger, P. Mansky, and T. P. Russell, Science **273**, 931 (1996).
[13] P. Mansky, J. DeRouchey, T. P. Russell, J. Mays, M. Pitsikalis, T. Morkved, and H. Jaeger, Macromolecules **31**, 4399 (1998).
[14] C. Harrison *et al.*, Macromolecules **33**, 857 (2000).
[15] J. Heier, E. J. Kramer, S. Walheim, and G. Krausch, Macromolecules **30**, 6610 (1997).
[16] R. D. Peters, X. M. Yang, T. K. Kim, B. H. Sohn, and P. F. Nealey, Langmuir **16**, 4625 (2000).
[17] S. P. Gido, J. Gunther, E. L. Thomas, and D. Hoffman, Macromolecules **26**, 4506 (1993).
[18] S. P. Gido and E. L. Thomas, Macromolecules **27**, 6137 (1994).
[19] M. W. Matsen, J. Chem. Phys. **107**, 8110 (1997).
[20] R. R. Netz, D. Andelman, and M. Schick, Phys. Rev. Lett. **79**, 1058 (1997).
[21] D. L. Polis and K. I. Winey, Macromolecules **29**, 8180 (1996).
[22] D. L. Polis and K. I. Winey, Macromolecules **31**, 3617 (1998).
[23] L. Qiao and K. I. Winey, Macromolecules **33**, 851 (2000).
[24] V. K. Gupta, R. Krishnamoorti, J. A. Kornfield, and S. D. Smith, Macromolecules **29**, 1359 (1996).
[25] Z.-R. Chen and J. A. Kornfield, Polymer **39**, 4679 (1998).
[26] J. L. Zyrd and W. R. Burghardt, Macromolecules **31**, 3656 (1998).
[27] U. Zhang and U. Wiesner, J. Chem. Phys. **103**, 4784 (1995).
[28] B. S. Pinheiro and K. I. Winey, Macromolecules **31**, 4447 (1998).
[29] Y. Oono and M. Bahiana, Phys. Rev. Lett. **61**, 1109 (1988).
[30] M. Bahiana and Y. Oono, Phys. Rev. A **41**, 6763 (1990).
[31] Y. Shiwa, T. Taneike, and Y. Yokojima, Phys. Rev. Lett. **77**, 4378 (1996).
[32] S. Qi and Z. G. Wang, Phys. Rev. Lett. **76**, 1679 (1996).
[33] S. Qi and Z. G. Wang, Phys. Rev. E **55**, 1682 (1997).
[34] H. Zhang, J. Zhang, Y. Yang, and X. Zhou, J. Chem. Phys. **106**, 784 (1997).
[35] S. R. Ren and I. W. Hamley, Macromolecules **34**, 116 (2000).
[36] T. Ohta, Y. Enomoto, J. L. Harden, and M. Doi, Macromolecules **26**, 4928 (1993).
[37] H. Kodama and M. Doi, Macromolecules **29**, 2652 (1996).
[38] M. Doi, J. L. Harden, and T. Ohta, Macromolecules **26**, 4935 (1993).
[39] F. Drolet, P. Chen, and J. Viñals, Macromolecules **32**, 8603 (1999).
[40] R. P. Huebener, *Magnetic Flux Structures in Superconductors* (Springer-Verlag, Berlin, 1979).
[41] M. Seul, L. R. Monar, L. O'Gorman, and R. Wolfe, Science **254**, 1616 (1991).
[42] M. Seul and D. Andelman, Science **267**, 476 (1995).
[43] Y. Oono and S. Puri, Phys. Rev. A **38**, 434 (1988).
[44] T. Ohta and K. Kawasaki, Macromolecules **19**, 2621 (1986).
[45] P. I. C. Teixeira and B. M. Mulder, Phys. Rev. E **55**, 3789 (1997), and references therein.
[46] D. Maring and U. Wiesner, Macromolecules **30**, 660 (1997).
[47] P. C. Hohenberg and B. I. Halperin, Rev. Mod. Phys. **49**, 435 (1977).
[48] P. G. de Gennes and J. Prost, *The Physics of Liquid Crystals* (Oxford University Press, Oxford, 1993), p. 165.
[49] I. W. Hamley, *Introduction to Soft Matter* (John Wiley, Chichester, 2000), p. 291.
[50] R. C. Ball and R. L. H. Essery, J. Phys.: Condens. Matter **2**, 10 303 (1990).
[51] T. Taneika and Y. Shiwa, J. Phys.: Condens. Matter **9**, L147 (1997).